



OPEN Design and development of a compact, wide-angle metamaterial electromagnetic energy harvester with multiband functionality and polarization-insensitive features

Najeeb Ullah^{1,2}, Md. Shabiul Islam^{1✉}, Ahasanul Hoque^{3✉}, Ahmed Alzamil⁴, Mohamed S. Soliman⁵ & Mohammad Tariqul Islam^{6✉}

This article presents a compact, wide-angle, polarization-insensitive metamaterial harvester that can efficiently harvest electromagnetic (EM) energy in the S, C, X, and Ku bands. The harvester's unit cell consists of a split ring resonator, two strip lines, and two split strip lines, giving it a total size of $(10 \times 10) \text{ mm}^2$. Each split gap is filled with a 50Ω resistive load. The input impedance of the harvester is precisely designed to match that of free space, allowing for efficient absorption of EM power and appropriate redirection towards the resistive loads. The harvester's performance is also evaluated for various polarization and incident angles, considering the Transverse Electric and Transverse Magnetic modes. The simulation results reveal that the proposed harvester exhibits a notably greater conversion efficiency of around $> 95\%$. The simulation outcomes were carefully validated through experimental tests conducted in an anechoic chamber using a 3×3 cell array of the proposed design. This ensured the accuracy and reliability of the results. The strong correlation between the experimental data and the full-wave simulations strongly supports the effectiveness of the proposed harvester. Therefore, the demonstrated efficiency and compact size make it a perfect fit for energy harvesting systems in wireless sensor networks.

Keywords Metamaterial, Electromagnetic energy harvesting, Polarization-insensitive

Wireless communication has become a vital element in the ever-changing realm of modern technology, significantly transforming how people connect and interact with their environment. Wireless Sensor Networks (WSNs) have driven technological advancements within the transformative paradigm. They have greatly facilitated the integration of wireless communication into numerous aspects of our daily lives. Environmental monitoring, healthcare, and industrial automation are just a few areas that have discovered their widespread use. The limitations of conventional power sources restrict the autonomy of wireless sensors, as they are naturally limited in supply¹. To effectively address the growing need for sustainable and self-sufficient energy systems, it is imperative to explore innovative solutions. With the increasing demand for energy and the urgent need

¹Faculty of Engineering (FOE), Multimedia University (MMU), 63100 Cyberjaya, Selangor, Malaysia. ²Faculty of ICT, BUIITEMS, Quetta 87300, Balochistan, Pakistan. ³Institute of Climate Change, Universiti Kebangsaan Malaysia, 43600 Bangi, Malaysia. ⁴Department of Electrical Engineering, College of Engineering, University of Ha'il, 81481 Ha'il, Saudi Arabia. ⁵Department of Electrical Engineering, College of Engineering, Taif University, 21944 Taif, Saudi Arabia. ⁶Department of Electrical, Electronic and Systems Engineering, Faculty of Engineering and Built Environment, Universiti Kebangsaan Malaysia, 43600 Bangi, Malaysia. ✉email: shabiul.islam@mmu.edu.my; ahasanul@ukm.edu.my; tariqul@ukm.edu.my

to adopt sustainable practices, there is a growing focus on researching and advancing inventive and efficient energy-harvesting technologies². Conventional power systems rely heavily on finite resources, resulting in adverse environmental impacts. Hence, it is imperative to shift towards alternative sources of energy. Energy harvesting is a concept that involves capturing energy from the surrounding environment and converting it into electrical power for practical purposes³. This approach has the potential to significantly increase the lifespan of wireless sensor nodes while also minimizing their environmental impact.

The study of metamaterials (MMs) holds great potential in pursuing sustainable energy solutions⁴. MMs are artificial structures endowed with electromagnetic (EM) characteristics that are absent in natural materials. These materials exhibit outstanding properties such as negative refraction and EM cloaking in their remarkable capacity to manipulate EM radiation. MMs possess distinctive attributes that render them an appealing and promising alternative for addressing the obstacles faced by conventional power systems.

Metamaterial absorbers (MMAs) represent a captivating and cutting-edge research domain within the MMs field. The materials with specific properties have been carefully engineered to interact with EM waves efficiently. Subwavelength structures, like resonators, are used to achieve remarkably high absorption efficiency within specific frequency ranges. MMAs have emerged as a promising technology that has the potential to revolutionize energy harvesting methods, particularly in applications such as wireless sensor networks. These absorbers are highly effective in capturing and dissipating EM energy, offering a distinct approach to enhance the efficiency and sustainability of power systems. This discovery marks a significant milestone in the quest for innovative, eco-friendly energy solutions.

Recent research has brought attention to the significant potential of MM perfect absorbers (MPA) in the field of energy harvesting applications^{5–7}. An EM energy harvesting application using MMs operating at 2.40 GHz, a widely used frequency band, was proposed in⁸. The design incorporated a square ring resonator that utilized resistors for power delivery. According to theoretical analysis, the energy harvesting efficiency (E-HE) was 83.6%. Furthermore, the study showcased the versatility of the temperature sensor configuration by demonstrating its applicability to a wide range of sensing applications beyond just energy harvesting. In⁹, researchers proposed an ultrathin dual-layer MMA for RF energy harvesting. This absorber consists of concentric annular structures made from copper foil on a flexible neoprene rubber sheet. The absorber exhibited three distinct absorption peaks at 1.75 GHz, 2.17 GHz, and 2.6 GHz, with 96.91%, 96.41%, and 90.12%, respectively. Numerical simulations and experiments have confirmed that the device exhibits robust RF performance in various conditions. This makes it a promising candidate for energy harvesting, as it demonstrates improved absorption values when subjected to different resistive loading scenarios. An absorber with concentric ring resonators is investigated in the research¹⁰, which demonstrates near-perfect absorption over a range of frequencies. Three efficiencies were proposed by analyzing the relationship between absorption characteristics and energy harvesting capability through numerical research on modifications in dimensions and geometry. The study focuses on multiband absorption and draws attention to converting half of the incoming wave energy (0.25 W) at 5.88 GHz utilizing resistive loads. This design has great promise for use in wireless communication and power systems. In¹¹, the authors conducted a study on RF energy harvesting for long-term power supply of electronic systems. They proposed a compact absorber based on a tilted split ring multiband MM. The absorber is designed to work effectively in LTE2350, WiFi2450, and LTE2600 frequency bands. It utilizes a split ring technique based on MM. The high-frequency structure simulator software simulations unveiled resonances at 2.35 GHz, 2.45 GHz, and 2.6 GHz frequencies. The corresponding return loss values were also obtained. The absorber's compact structure, measuring 35 mm × 35 mm × 1.67 mm, and its multiband features make it a highly promising solution for RF energy harvesting applications. A metasurface (MS) with two bands, one for 2.4 GHz and one for 5.4 GHz, was proposed in¹² for effective EM energy harvesting. With a circular split ring resonator on a low-loss substrate with an air layer, the MS unit cell could attain near-unity efficiency of 97% at 2.4 GHz and 94% at 5.4 GHz, respectively. The MS utilized a single harvesting port, simplifying the power network design. Experimental validation of a 5 × 5-unit cell MS harvester confirmed its high efficiency and suitability for diverse microwave applications, including energy harvesting and wireless power transfer. A MPA combined with Schottky diodes was developed in¹³ for harvesting high-efficiency radio frequency (RF) energy. By capitalizing on Fabry–Perot (FP) cavity resonance to enhance energy absorption, the MPA-based rectenna effectively converted RF waves to DC power. Particularly at low intensities, incorporating FP resonance increased the voltage and Q-factor across Schottky diodes, enhancing rectification efficiency. In¹⁴, the authors developed a perfect, triple-band MS absorber that efficiently harvests RF energy. The absorber was designed with a three-layer meta-atom structure of cross-shaped and slotted square-shaped metallic patches. In total, there were 9 × 9 meta-atoms in the design. This absorber could operate in both S- and C-bands, with resonant frequencies at 3.06, 3.9, and 5.97 GHz. The experiment demonstrated nearly perfect absorption at various incident angles, and the results closely matched the simulations. The absorber demonstrated a high E-HE, achieving 94.4% and 84% at frequencies of 3.07 and 5.97 GHz, respectively. The MMA described by the authors in¹⁵ featured resistive loads and a multi-type split coin resonator. The design mentioned above demonstrated angle insensitivity by attaining an absorption efficiency of over 80% for transverse EM waves within the frequency range of 3 to 8 GHz. A blend of experimental validations and numerical simulations supported the conclusions drawn by the researchers. The absorber was effectively utilized in energy harvesting applications, demonstrating significant efficiencies in absorption (82.21%) and harvesting (46.07%). A MMA structure designed for microwave energy harvesting was proposed in¹⁶. The structure was comprised of four-wheel resonators, each possessing distinct dimensions. The chosen frequency range corresponds to the commonly used wireless communication signals. The dimensions were optimized for achieving a wideband absorption response through the utilization of a parametric study and genetic algorithm. Study results showed substantial absorption ratios in the 3–5.9 GHz and 7.3–8 GHz frequency ranges, with values ranging from 80 to 99%. Furthermore, the E-HE in the 2–5 GHz range surpassed 0.8, indicating a highly effective process. In¹⁷, the authors proposed an MS for energy harvesting applications. Their design was

composed of subwavelength electrical small ring resonators operating at 2.5 GHz. The resonators were organized in a two-dimensional array, which allowed for efficient energy harvesting. The MS demonstrated 90% E-HE when subjected to varying polarization and incidence angles. A 9×9 MS energy harvesting array prototype was manufactured and tested, and its efficiency for incident waves with arbitrary polarizations and broad angle was found to be over 80%.

Extensive research in EM harvesting utilizing MMs has propelled the field forward significantly. However, it is imperative to acknowledge the inherent constraints and limitations within current designs. It is worth mentioning that certain designs result in MMs structures that are quite large^{8–17}, making them unsuitable for applications with strict size and weight limitations. Additionally, many existing designs are confined to a limited range of absorption frequency bands^{8,13,17}, restricting their capacity to harness energy from a broader spectrum of EM waves and diminishing overall versatility. In addition, it is necessary to focus on developing smaller, more flexible, and more efficient MMs structures for EM energy harvesting applications.

This study introduces a new energy harvester, measuring 10×10 mm², based on MMs. Its compact size not only helps to reduce costs but also enhances manufacturability. Additionally, its compact design allows for precise and cost-effective fabrication. The product seamlessly integrates into current systems, improving their portability and versatility. This broadens the range of applications and fosters innovation in MM technology.

Furthermore, the MM harvester's multiband functionality enables it to efficiently capture energy from different frequency bands simultaneously, maximizing its utilization of ambient EM waves. This adaptability makes it perfect for urban environments with crowded communication networks, enabling strong and self-sufficient wireless sensor networks and IoT devices. It emphasizes energy efficiency and sustainability by minimizing the need for frequent battery replacements or wired power sources, benefiting a wide range of technological applications.

The proposed energy harvester has four resonance frequencies at 3.7 GHz, 6.3 GHz, 9.9 GHz, and 14.2 GHz. The design effectively showcases negative (permittivity and permeability) within specific frequency ranges. It is firmly established as a double negative (DNG) MM. The energy harvester demonstrates exceptional absorption efficiencies across multiple frequencies. The absorption efficiency at 3.7 GHz is remarkably high, reaching 99.96%. At frequencies of 6.3 GHz, 9.9 GHz, and 14.2 GHz, the absorption efficiencies are 99.87%, 99.88%, and 99.87%, respectively. The proposed structure has shown its effectiveness in capturing EM power from different incident angles, as evidenced by computational simulations and experimental results. The EM harvesting efficiency reaches 95.3% at 3.7 GHz. At 6.3 GHz, 9.9 GHz, and 14.2 GHz, it attained 96.5%, 95%, and 95.2% under normal incidence, respectively. Our novel energy harvester has distinct advantages over established methodologies, making it highly valuable in practical applications. Our design has the potential to revolutionize various industries, making it highly appealing.

Design layout

The resonators within each layer exhibit resonance at frequencies that are closely spaced but distinct from one another due to variations in their dimensions. By combining the overlapping frequency responses of each layer, one can determine the overall response of the structure¹⁸. Moreover, the design's absorption and frequency response depend upon several aspects. These criteria encompass the number of resonators, their geometric measurements, the widths, and the diameters of the split gaps¹⁹.

The front and back views of the proposed unit cell design layout are shown in Fig. 1a and b. Additionally, Fig. 1c displays the design layout of the 3×3 array structure. The unit cell consists of a split ring resonator (SRR), two strip lines, and two split strip lines. The strip lines that connect the ring's edges are the same width. The inner split strips, which have the same widths, are connected to the middle of the ring resonator. The resonators are made of annealed copper, with a thickness of 0.035 mm and a conductivity (σ) of 5.8×10^7 S/m. The split gaps are connected to the lumped elements (resistive loads), specifically R1, R2, and R3. The proposed unit cell has an overall size of (10×10) mm², while the 3×3 array structure has a size of (30×30) mm². Compared to other designs documented in the literature, the proposed one is comparatively smaller. Furthermore, the split ring resonator's 45° inclination is another distinguishing characteristic of the design, significantly enhancing its bandwidth.

Furthermore, the dielectric loss tangent measures the loss level in a dielectric substance. It demonstrates how EM energy within the material is turned into heat. Consequently, RF losses are more significant, and the absorption bandwidth is broader due to a higher loss tangent, which signifies a greater amount of energy being lost²⁰. Consequently, the Rogers RT 5880 substrate is employed in the proposed design to reduce energy losses effectively. The substrate's permittivity (ϵ) is 2.2, and its loss tangent (δ) is 0.0009. It has a thickness of 1.575 mm. Table 1 displays the optimal structure dimensions as obtained by a parametric study.

A parametric analysis was conducted to ascertain the configuration of the top-layer metal pattern. The Scattering parameters were evaluated using five separate designs. The final design met all the required characteristics, which dictated the top layer's shape. Figure 2 illustrates the various designs of top-layer structures, whereas Fig. 3 shows the S11 values for these designs.

The proposed device's equivalent circuit model is constructed in ADS, and its outcomes are compared to those obtained by CST. Figure 4 depicts the equivalent circuit model. Furthermore, Fig. 5 presents the Scattering parameters data for the ADS and CST. Figure 5 shows a remarkable resemblance in the S11 values between CST and ADS values.

Furthermore, as illustrated in Fig. 6, the scattering parameters were examined using two distinct substrate materials: Rogers RT 5880 and FR4. The S11 results are optimized for Rogers RT 5880 due to its lower loss tangent than FR4. As a result, the substrate chosen for the proposed device was Rogers RT 5880.

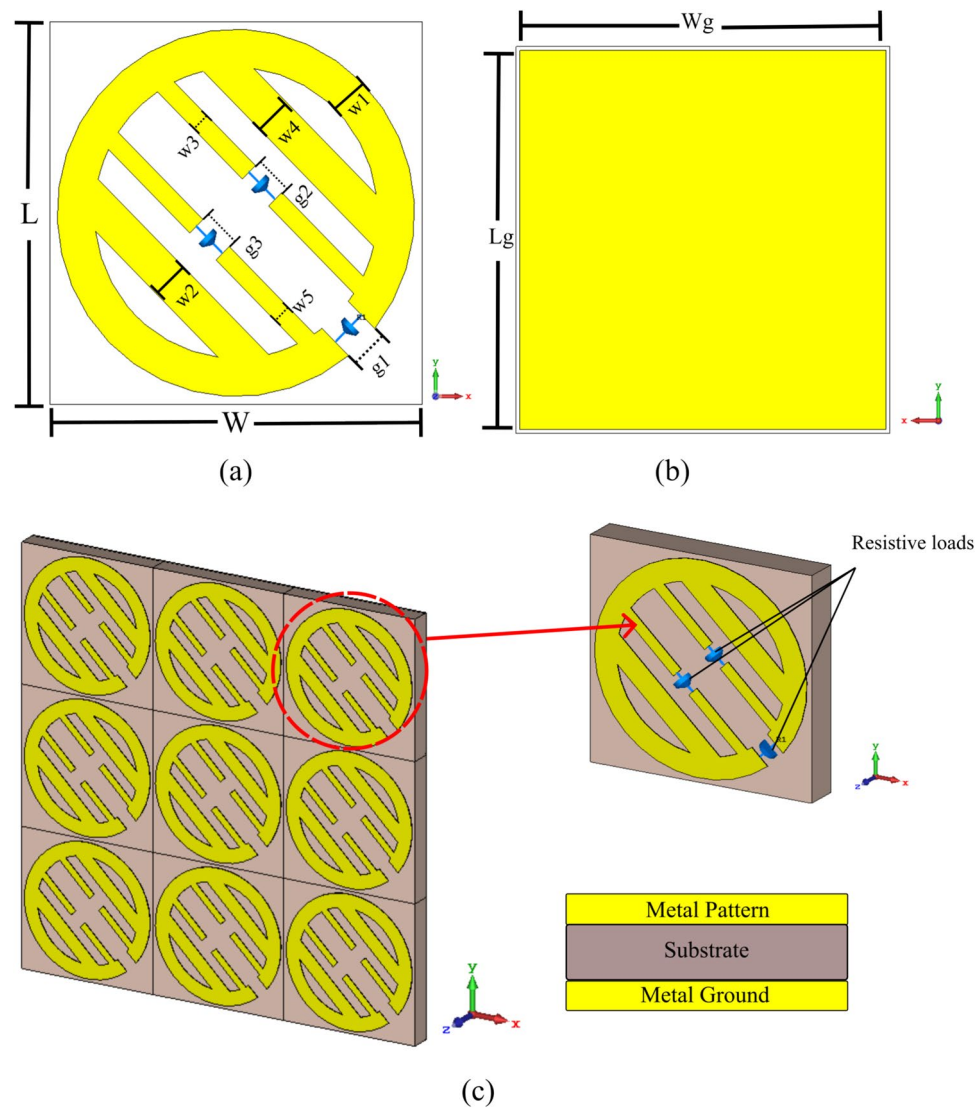


Figure 1. Schematic structure (a) Unit cell front-view (b) Unit cell Back-view c Prospective view of 3 × 3 array structure.

Parameters	Dimension (mm)	Parameters	Dimension (mm)
L	10	W3	0.5
W	10	W4	1
Lg	9.8	W5	0.5
Wg	9.8	g1	1
W1	1	g2	1
W2	1	g3	1

Table 1. The geometric dimensions of the proposed structure.

Analysis of the proposed harvester’s absorption and scattering parameters

The numerical simulations use Microwave Studio, a Computer Simulation Technology (CST) software. CST provides investigations in the microwave frequency band utilizing genetic and parametric algorithms. Each of the three axes represents different boundary conditions: electric, magnetic, and open. We assume the E-field and H-field components are x- and y-polarized to facilitate numerical analysis. Furthermore, it is postulated that the propagation occurs in the z-direction. The absorption of the proposed unit cell is calculated using the equation below²¹.

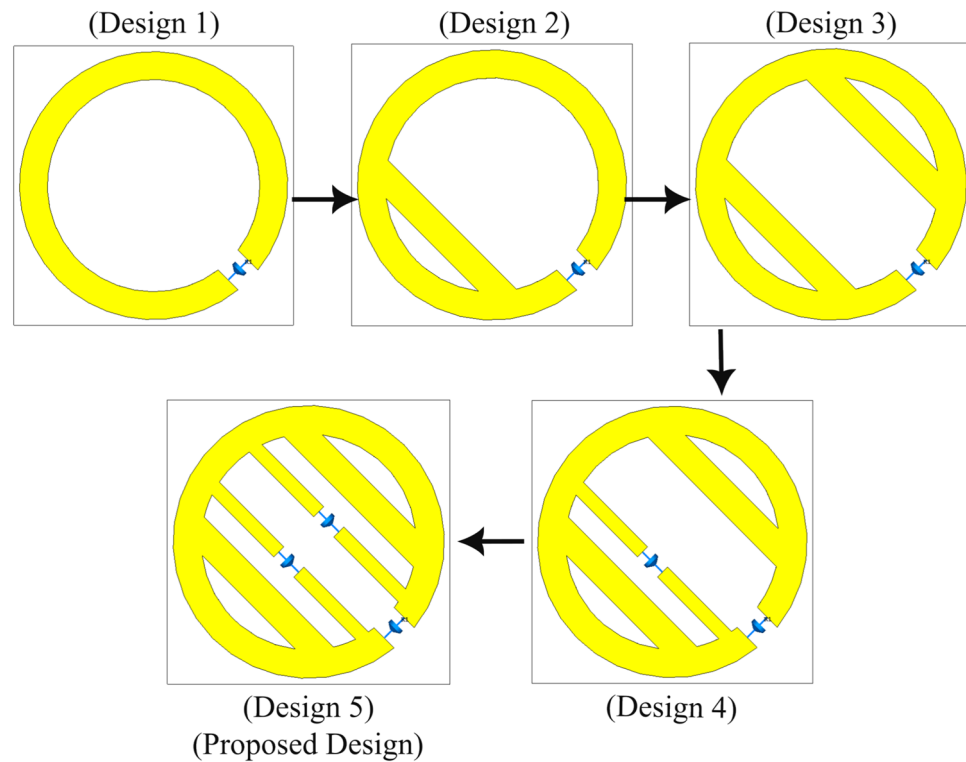


Figure 2. Parametric analysis of the proposed design.

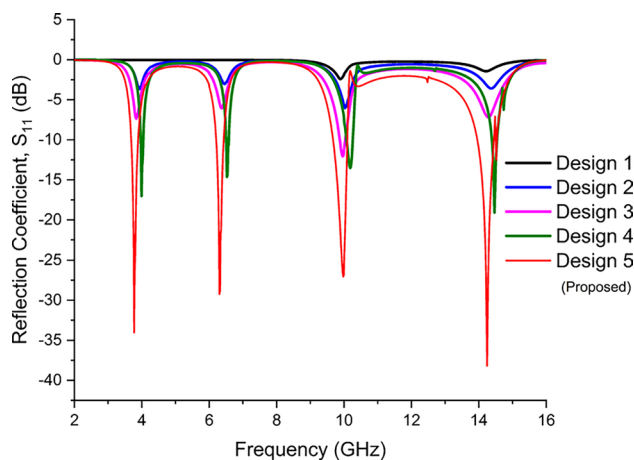


Figure 3. Reflection coefficient (S_{11}) for various designs.

$$A(\omega) = 1 - |S_{11}(\omega)|^2 - |S_{21}(\omega)|^2 \quad (1)$$

where $S_{11}(\omega)$ denotes the overall structure's reflection coefficient and $S_{21}(\omega)$ denotes its transmission coefficient. To optimize the absorption of structure, it is important to minimize both the reflection $S_{11}(\omega)$ and the transmission $S_{21}(\omega)$ at the operating frequency. As the backside of the back layer is entirely covered with copper, the absorption coefficient may be determined using the following equation:

$$A(\omega) = 1 - |S_{11}(\omega)|^2 \quad (2)$$

The following equations can be used to compute the scattering parameters, specifically the reflection coefficient (S_{11}) and the transmission coefficient (S_{21})²²:

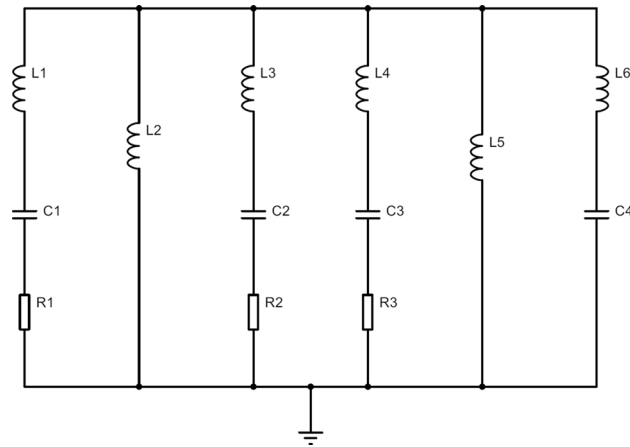


Figure 4. The equivalent circuit model of the proposed MM harvester.

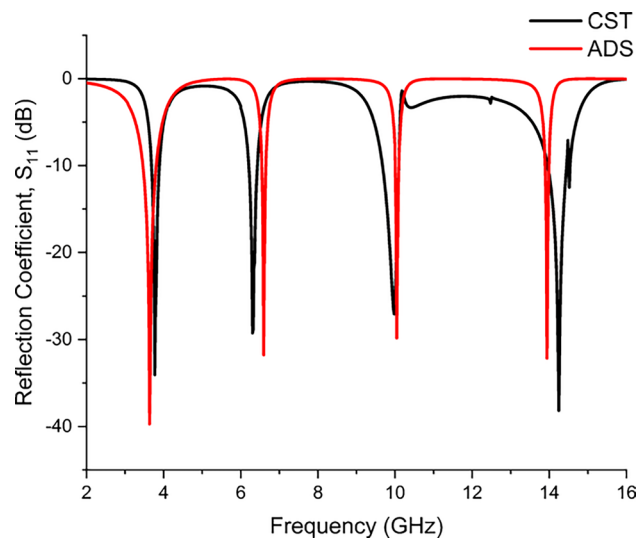


Figure 5. Reflection coefficient from CST and ADS.

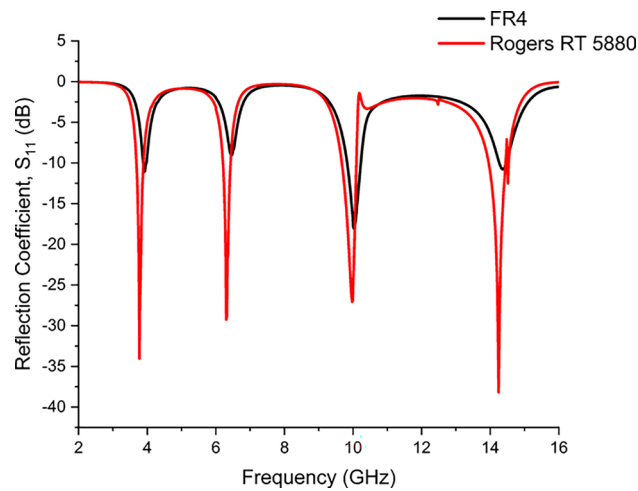


Figure 6. Reflection coefficient for FR4 and Rogers RT 5880.

$$S_{11} = \frac{R_{01}(1 - e^{i2nk_0d})}{1 - R_{01}^2 e^{i2k_0d}} \quad (3)$$

$$S_{21} = \frac{(1 - R_{01}^2)e^{ink_0d}}{1 - R_{01}^2 e^{i2k_0d}} \quad (4)$$

where $R_{01} = z - 1/z + 1$. The impedance, represented by the symbol z , can be determined through the utilization of the following equation:

$$z = \pm \sqrt{\frac{(1 + S_{11})^2 - S_{21}^2}{(1 - S_{11})^2 - S_{21}^2}} \quad (5)$$

$$e^{ink_0d} = X \pm i\sqrt{1 - X^2} \quad (6)$$

$$X = \frac{1}{2S_{21}(1 - S_{11}^2 + S_{21}^2)} \quad (7)$$

Figure 7 displays the simulated results for S_{11} and S_{21} , respectively. Four resonance frequencies are depicted in the Figure: 3.7 GHz, 6.3 GHz, 9.9 GHz, and 14.2 GHz. At these resonance frequencies, the S_{11} values are −34 dB, −29 dB, −27 dB, and −38 dB, respectively. The S_{21} values are −0.10 dB, −0.16 dB, −0.20 dB, and −0.13 dB. The N5227A model of a Vector Network Analyzer (VNA) is utilized to evaluate the S-parameters and validate the simulation results. The VNA was prepared using the calibration kit (Agilent N4694-60001). After careful consideration, a waveguide was selected to operate effectively within the 2–16 GHz frequency range. Two coaxial cables, one for transmission and one for reception, connected the VNA to the waveguides. Five distinct waveguide models were considered to find the S-parameters. The unit cell is inserted into these waveguides sequentially. The PRN file format was used to record the measured values for S_{11} and S_{21} obtained from the VNA. The graph plotting process was completed by importing the (PRN) data into Excel and Origin. The measurement setup is illustrated in Fig. 8a, and the fabricated unit cell and array structure is shown in Fig. 8b. Figure 9 presents the simulated and measured S_{11} .

The absorption of the proposed unit cell with lumped elements is calculated using Eq. (2). Figure 10 illustrates the absorption of the proposed unit cell at four distinct resonance frequencies. The absorption rate is 99.96% at 3.7 GHz, 99.87%, 99.88%, and 99.87% at 6.3 GHz, 9.9 GHz, and 14.2 GHz, respectively. Nearly perfect absorption and near-zero reflection are observed at the four resonance frequencies.

The analysis of the absorption of an MM harvester in different Transverse Electric (TE) and Transverse Magnetic (TM) modes for energy harvesting presents significant advantages. This computational method enhances the design of the harvester, guaranteeing maximum energy conversion efficiency by precisely adjusting its interaction with various modes. The ability to customize to a higher degree allows for tailored adaptation to specific operating conditions. This is crucial for achieving optimal performance in various environments and addressing variations in EM waves.

Figures 11 and 12 depict the absorption responses of the proposed design for TE and TM modes. The incident angles (θ_{inc}) vary from 0° to 75°, with a step size of 15°. In the case of TE and TM modes, the polarization angle (ϕ) remains fixed at 0°. In TE mode, the electric field (E-field) is perpendicular to the direction of wave

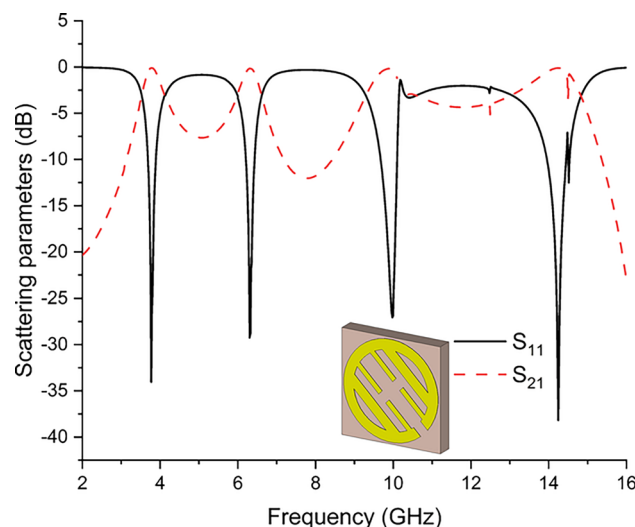


Figure 7. Scattering parameters, S_{11} and S_{21} vs frequency.

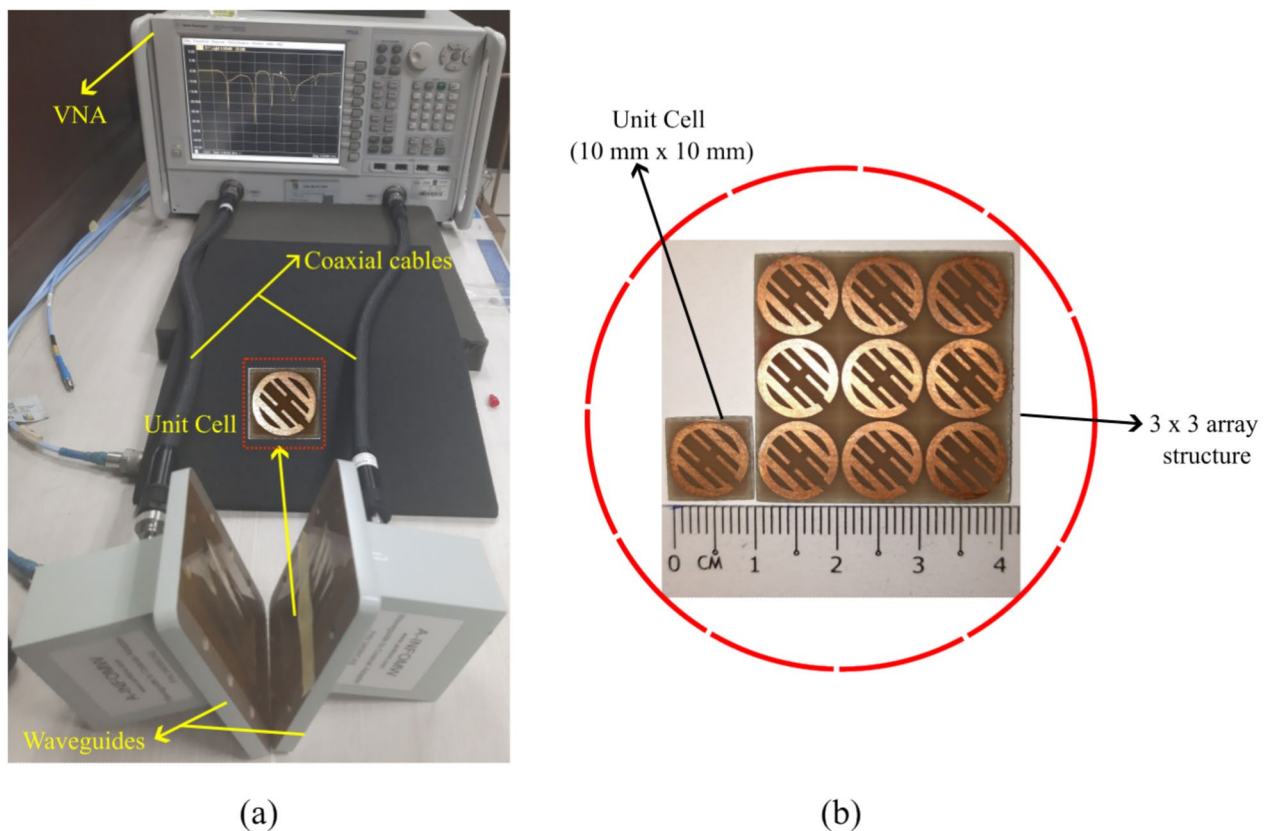


Figure 8. (a) Measurement setup for a unit cell using a vector network analyzer (VNA). (b) Fabricated unit cell and array structure.

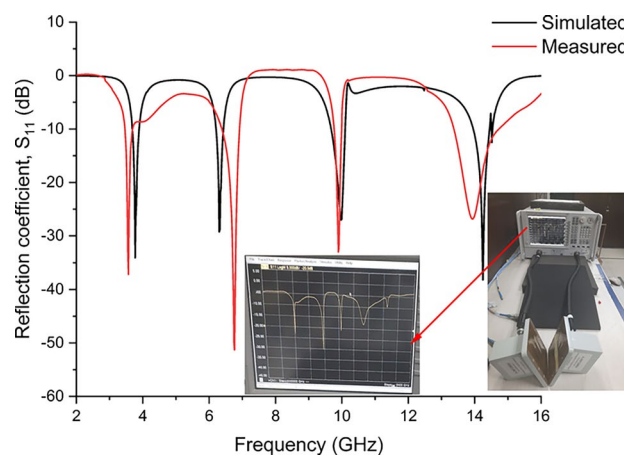


Figure 9. The measure and simulated reflection coefficient, S_{11} (dB) versus frequency (GHz).

propagation and remains fixed in that perpendicular plane. In contrast, the magnetic field (H-field) has components that are perpendicular and parallel to the direction of wave propagation.

Conversely, in TM mode, the magnetic field (H-field) is perpendicular to the direction of wave propagation. It remains fixed in that perpendicular plane, while the electric field (E-field) exhibits both perpendicular and parallel components to the direction of wave propagation. The figures show that the absorption responses from 0° to 45° are almost identical to those at 0° . However, as the incident angle increases from 45° to 60° and 75° , there is a clear reduction in absorption and a shift in the resonance point.

To optimize the performance, versatility, and reliability of MM harvesters, it is crucial to investigate the absorption responses at various polarization angles. Ensuring they can perform effectively in multiple applications and operating conditions is essential. Figure 13 illustrates the effect of changing the polarization angle (ϕ) on the absorption response when the incidence is normal. The absorption remains constant for the polarization

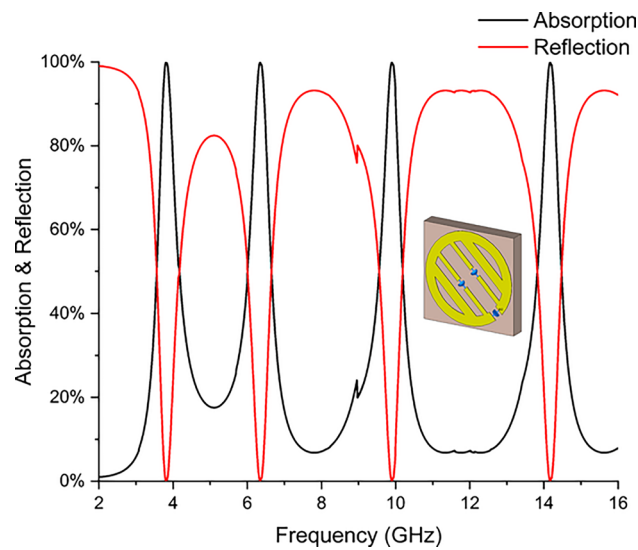


Figure 10. Absorption & reflection of the proposed unit cell with resistive loads at four distinct resonance frequencies.

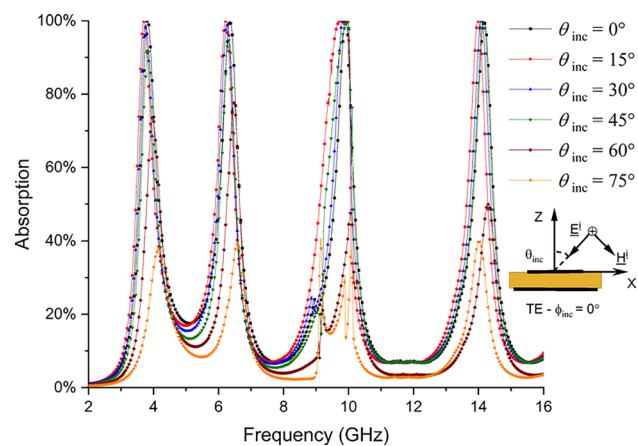


Figure 11. Absorption in (%) versus frequency for varying incident angles (θ_{inc}) (TE-polarization mode).

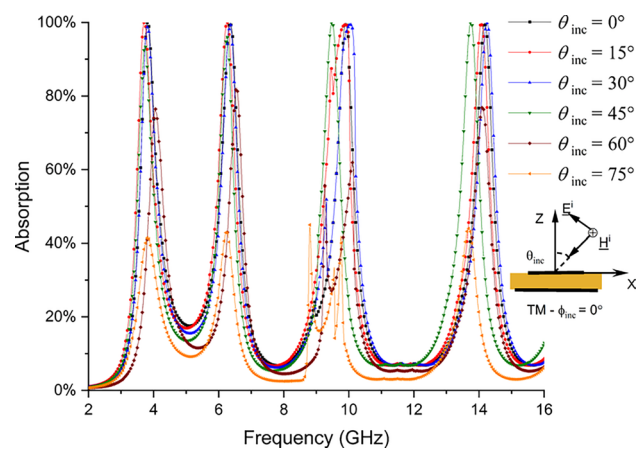


Figure 12. Absorption in (%) versus frequency for varying incident angles (θ_{inc}) (TM- polarization mode).

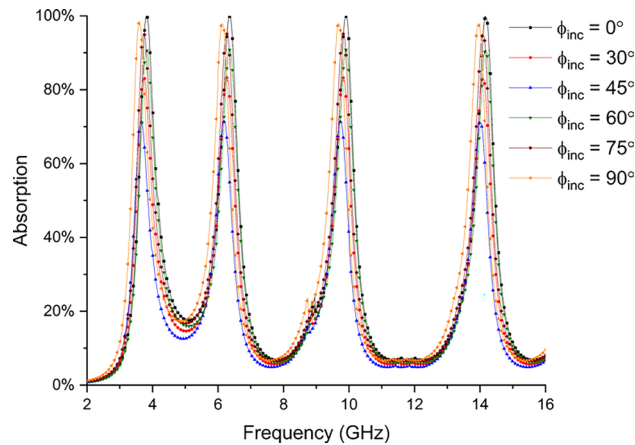


Figure 13. Absorption versus frequency for varying polarization angles (ϕ) under normal incident.

angles of 75° and 60°. Nevertheless, for angles of 15°, 30°, and 45°, there is a minor reduction in the extent of absorption and a modest change in the frequency at which resonance occurs. In general, the proposed MM harvester seems to be impervious to polarization.

Assessment of the proposed design's E-HE

The simulated E-HE of the MM was calculated using CST Studio Suite. The simulation required the creation of a three-dimensional model that included specific parameters and detailed specifications for incident wave properties. The simulated E-HE (η) in percentage can be calculated using the equation below:

$$\eta = \left(\frac{P_{load}}{P_{incident}} \right) \times 100 \quad (8)$$

Therefore, the total power delivered to the loads is denoted by, $P_{load} = P_{absorbed} - P_{loss}$. Meanwhile, $P_{incident}$ represents the whole incident energy that the MM device received at that time. Figure 14 shows the proposed design's simulated E-HE. The efficiency at 3.7 GHz is 95.2%, while at 6.3 GHz, 9.9 GHz, and 14.2 GHz, it is 94.84%, 96.11%, and 94.41%, respectively. Figure 15 presents a detailed analysis of the power delivered to loads for TE modes, considering oblique incidence angles ranging from 0 to 60°. The Figure demonstrates the power transfer efficiency to the load, highlighting its remarkable effectiveness. The transfer process demonstrates high efficiency, with minimal dissipation within the copper and dielectric substrate. The device shows exceptional efficiency at normal incidence (0°), exceeding 95%, indicating its superior performance under standard conditions. In addition, the study's findings demonstrate a sustained level of optimal performance, even when the angle of incidence is raised to 45°. Nevertheless, once the incident angle reaches 60°, there is a noticeable decline in efficiency. This observation indicates a potential drawback in the device's performance when used at higher incidence angles, emphasizing the significance of taking the angle of incidence into account when aiming to enhance power transfer efficiency.

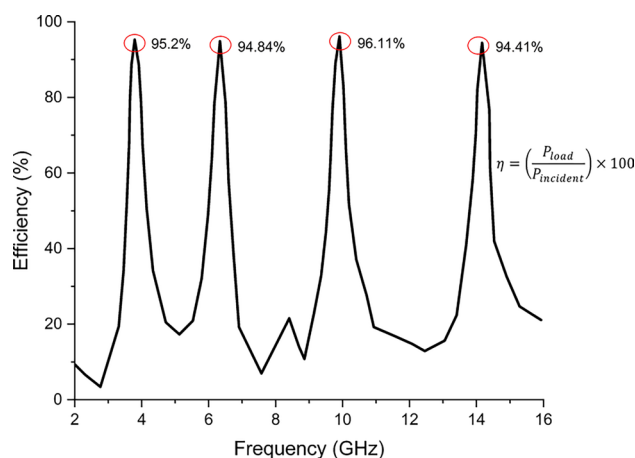


Figure 14. Simulated E-HE versus frequency.

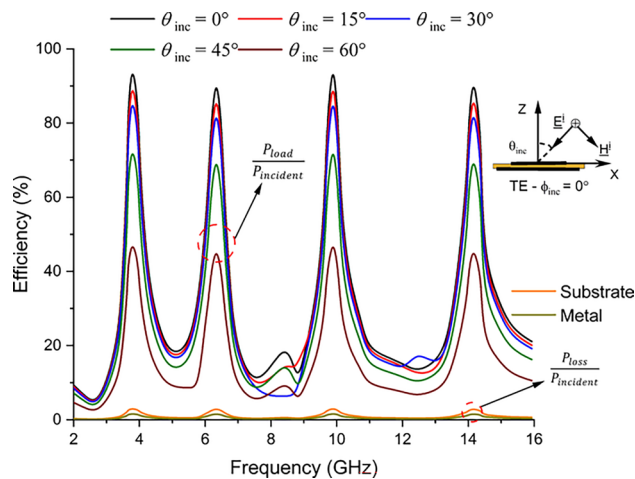


Figure 15. Simulated E-HE for varying incident (θ_{inc}) angles (TE-polarization mode).

Integrating the lumped elements (*resistive loads*) is vital in designing the EM energy harvester. The study examines the effectiveness of harvesting by adjusting the resistive loads connected from (50 to 200 Ω), as depicted in Fig. 16. The unit cell demonstrates an impressive efficiency of nearly 95% when connected to a resistor load of 50 Ω , almost identical to the input impedance of the proposed harvester. In addition, the efficiency exceeds 85% at all resonant frequencies for resistive loads of 100 Ω . For resistive loads of 150 Ω and 500 Ω , the efficiency is 80% and 65%, respectively.

It is critical to conduct precise measurements of the magnetic field (H-field), surface current, and electric field (E-field) of an MM harvester to analyze its functionality, refine its design, and resolve any potential problems. These measurements serve multiple purposes, including identifying hotspots, validating simulation models, and customizing the harvester for various conditions. This enhances the versatility of the harvester. The analysis conducted here thoroughly comprehends the EM phenomena within the structure at different resonance frequencies.

The current distribution at resonance frequencies is independently measured in Fig. 17, which reveals an anti-parallel current flow. An intense current is generated in the outer SRR at a frequency of 3.7 GHz. The current is focused in the center and then sent to the resistor load, resulting in almost perfect absorption. At a frequency of 6.3 GHz, the inner two split strip lines show a significant increase in current intensity. Similarly, at 9.9 GHz and 14.2 GHz frequencies, the corner strip lines demonstrate elevated current levels.

In Fig. 18, the E-field distributions exhibit clear and distinct patterns at the resonance frequencies. At a frequency of 3.7 GHz, both outer SRR and inner split strip lines demonstrate a high concentration of E-field intensity. When transitioning to a frequency of 6.3 GHz, the E-field is concentrated within the inner split strip lines that contain resistive loads. At a frequency of 9.9 GHz, the concentration of the E-field shifts towards the

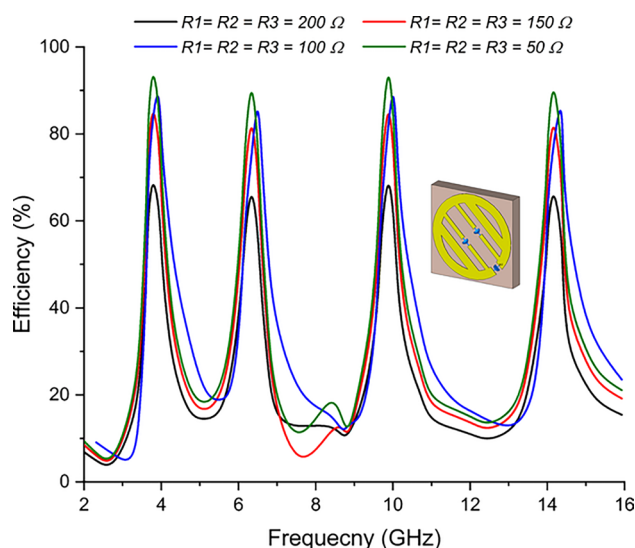


Figure 16. Efficiency vs. frequency for different resistive loads.

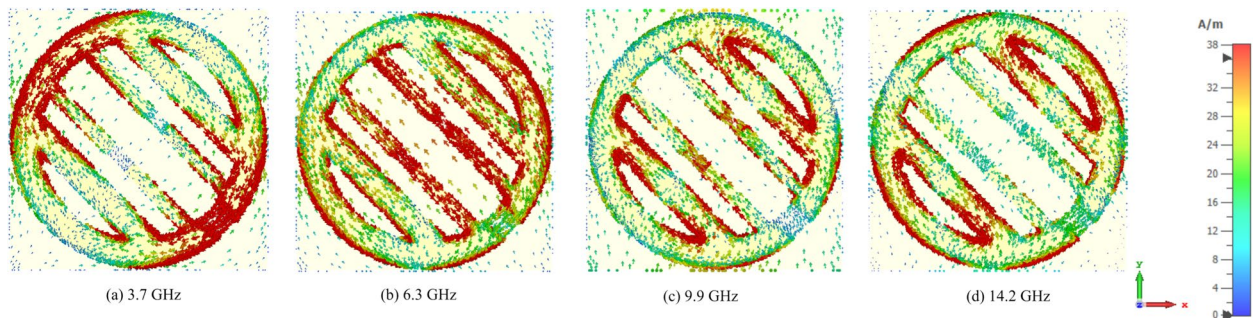


Figure 17. Surface current distribution at all four resonance frequencies.

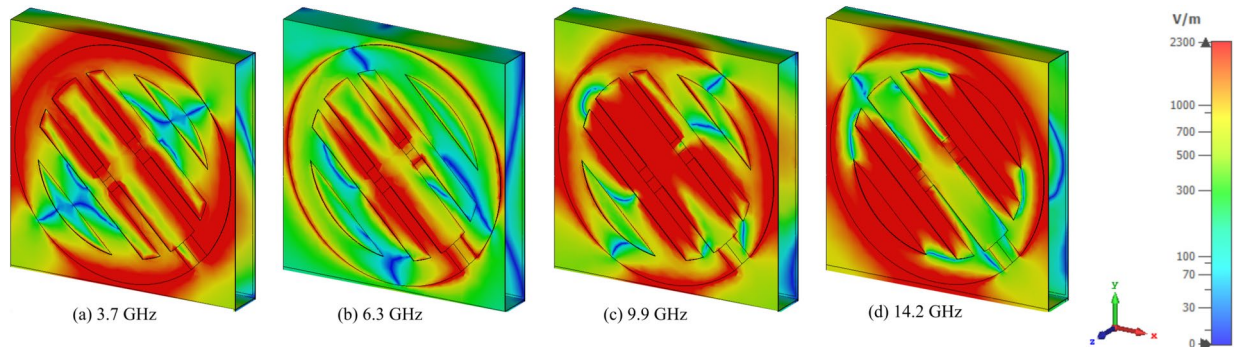


Figure 18. Distribution of the E-field at each of the four resonance frequencies.

inner split strip lines and outer SRR. Similarly, at a frequency of 14.2 GHz, both the corner strip lines and outer SRR exhibit an intensified E-field.

Figure 19 provides additional analysis by presenting H-field distributions. Significant fields are observed at the inner split strip lines, particularly at a resonance frequency of 3.7 GHz and 6.3 GHz. At a frequency of 6.3 GHz, the outer SRR demonstrates concentrated fields on the lower side. At a frequency of 9.9 GHz, the H-field intensity becomes concentrated in the upper and lower sides of the inner split strip lines. At a frequency of 14.2 GHz, the corner strip lines exhibit the highest intensity of the H-field.

The proposed design undergoes initial validation through simulations and subsequent experimental verification using the fabricated 3×3 array structure. Figures 20 and 21 show the schematic diagram and experimental setup, respectively. The efficiency of the array structure is determined through a comprehensive evaluation conducted in an anechoic chamber. The experimental setup ensures that external interference is kept to a minimum, which enables precise measurements of the array's performance. The experiment utilized an RF signal generator, spectrum analyzer, horn antennas, and adapters. The input ports of the horn antenna were connected to the signal generator to guarantee that it could produce the correct frequency for testing. Next, a spectrum analyzer measured the received power after the array was attached to the transmitting horn antenna and positioned in the far-field zone. Equation (9) can be used to calculate the necessary separation distance between the transmitter antenna and the array sample for optimal excitation of the array by a plane wave in the far-field area²³:

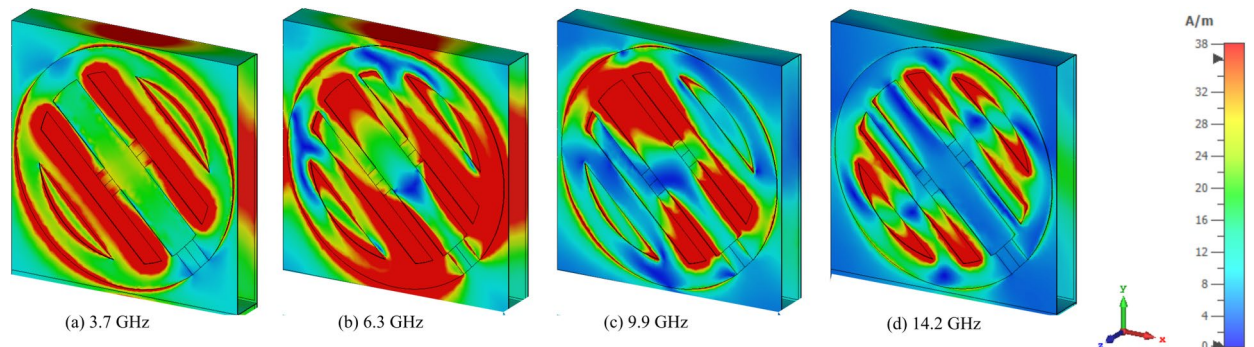


Figure 19. Distribution of the H-field at each of the four resonance frequencies.

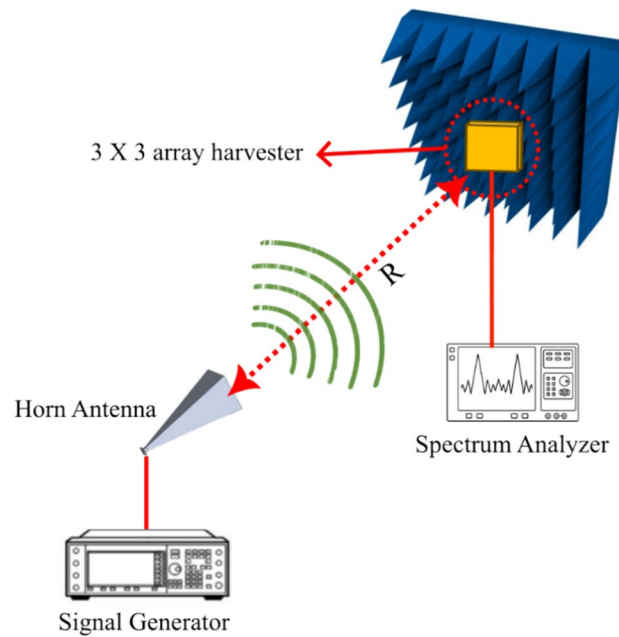


Figure 20. Schematic diagram of the measurement setup for the 3×3 array harvester in an anechoic chamber.

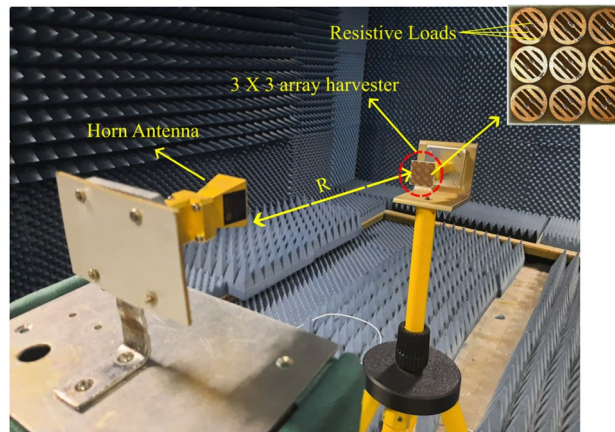


Figure 21. The actual measurement setup for the 3×3 array harvester inside an anechoic chamber.

$$R = \frac{2D^2}{\lambda} \quad (9)$$

Concerning this context, R denotes the distance between the array sample and the horn antenna, D represents the aperture of the antenna, and λ denotes the wavelength. Using the following equation, we can get the array structure's total RF-to-AC efficiency²⁴:

$$\eta_{(RF-AC)} = \frac{P_{load}}{P_{incident}} \times 100 \quad (10)$$

$$P_{load} = \sum_{n=1}^N V_i^2 / R_i \quad (11)$$

The voltage across the resistance of each collector is denoted as V_i , is determined by R_i , while N represents the total number of cross-dipole elements.

$$P_{incident} = P_t G_t \left(\frac{A}{4\pi R^2} \right) \quad (12)$$

P_t and G_t indicate the power and gain of the transmitting antenna, respectively, whereas A represents the functional surface area of the unit cell perpendicular to the incidence plane.

The array structure's simulated and measured E-HE under normal incidence is shown in Fig. 22. The peak efficiency of the measure was 95.3% at 3.7 GHz. At 6.3 GHz, 9.9 GHz, and 14.2 GHz, it reached 96.5%, 95%, and 95.2%, respectively. The fabrication process, measurement port losses, and calibration errors indicate a slight discrepancy between the simulated and measured outcomes. Overall, the results strongly agree with the measurement data and the simulation outputs.

Due to several important factors, using a Rogers 5880 substrate and copper resonator dramatically improved our harvesting system. Rogers 5880's low dielectric constant and loss tangent reduce energy loss. However, copper's high electrical conductivity reduces resistive losses and optimizes energy transfer. Rogers 5880's thermal stability and dielectric properties ensure reliable operation in various temperature and frequency settings. Advanced fabrication procedures compatible with Rogers 5880 allow accurate copper resonator patterning, improving MM EM characteristics. This combination enables optimal impedance matching, reducing reflection losses and maximizing E-HE.

Furthermore, the power efficiency is calculated using the following equation²⁵:

$$\text{Efficiency} = \frac{P_{harvested}}{P_{transmitter}} \times 100 \quad (13)$$

$$P_{harvested} = P_{received} \times \eta \quad (14)$$

$$P_{received} = P_{transmitter} - FSPL \quad (15)$$

where η is the efficiency of the MM array at the respective resonance frequency. The Free Space Path Loss (FSPL) is determined using the equation below²⁶:

$$FSPL = 20\log_{10}(d) + 20\log_{10}(f) + 20\log_{10}\left(\frac{4\pi}{c}\right) \quad (16)$$

The distance between the transmitter and the receiver is denoted by d , measured in meters; the frequency is represented by f , measured in Hz, and the speed of light is denoted by c , equal to 3×10^8 m/s.

Figure 23 illustrates the power efficiency at four distinct resonance frequencies, measured at varying distances ranging from 0.5 to 2 m. This distance represents the separation between the signal source and the harvester device. The power efficiency is significant up to 1 m.

Table 2 compares the proposed harvester to other efforts in the field and gives a thorough description of its features and performance. The proposed harvester showcased a more compact design and improved E-HE in comparison to previously published research works^{14,17,27–36}. Despite the smaller sizes of the works presented in³⁷ and³⁸, their E-HE is lower than the efficiency achieved by the proposed harvester.

Conclusion

This article presents a compact, wide-angle, and polarization-insensitive MM harvester with multiband. The harvester underwent a comprehensive numerical analysis using CST Microwave Studio, revealing a superior absorption ratio, excellent angular stability, and enhanced efficiency at resonance frequencies (3.7 GHz, 6.3 GHz,

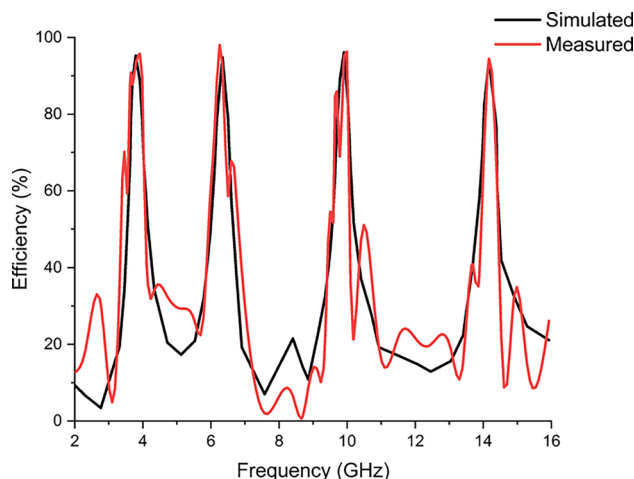


Figure 22. Comparison of simulated and measured E-HE of the proposed harvester.

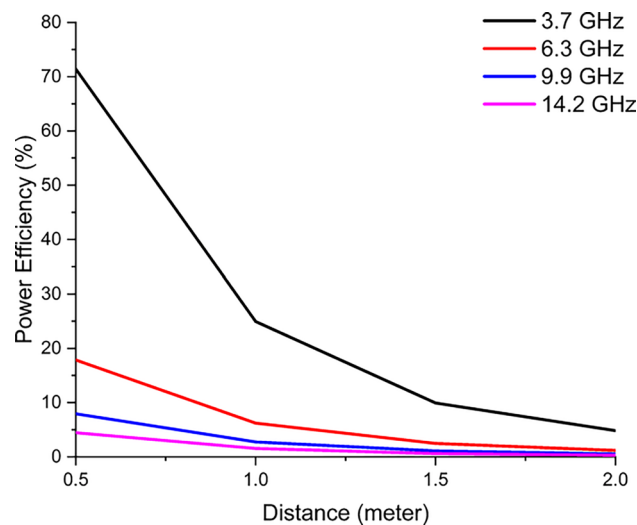


Figure 23. Power efficiency (%) versus distance (meter).

References	Dimension of the unit cell	Substrate used	Frequency (GHz)	Measured energy harvesting efficiency η (%)	Cost	Complexity
14	$0.32 \lambda_0$	FR4	3.06,3.9, and 5.97	94.4 and 84	High	Simple
17	$0.13 \lambda_0$	F4B	2.5	90	Medium	Simple
27	$0.08 \lambda_0$	Rogers RT/duroid 6006	2.45 and 6	90 and 85	Medium	Medium
28	$0.123 \lambda_0$	Rogers TMM10	2.45	96.5	Medium	Simple
29	$0.22 \lambda_0$	Rogers RO4350B	5.54	91	Medium	Simple
30	$0.13 \lambda_0$	Rogers 3210	2.4, and 5.8	58 and 51	Medium	Medium
31	$0.3 \lambda_0$	Rogers RO4350	5.8	93.1	High	Complex
32	$0.56 \lambda_0$	RT/duroid 5880 Rogers	2.4	70	High	Simple
33	$0.32 \lambda_0$	None	5.8	88	Medium	Complex
34	$0.6 \lambda_0$	Rogers RO4003C	2.45	61	Medium	Simple
35	$0.15 \lambda_0$	Rogers 4003C	2.66, 5.40, 6.298	None	Medium	Medium
36	$0.16 \lambda_0$	PTFE	2.45	97.3	High	Medium
37	$0.13 \lambda_0$	Rogers RO3010	5.33	86	Low	Complex
38	$0.11 \lambda_0$	Rogers RO4003C	5.5 and 7.2	None	Low	Medium
This work	$0.12 \lambda_0$	Rogers RT 5880	3.7, 6.3, 9.9, and 14.2	95.3, 96.5, 95, and 95.2	Low	Simple

Table 2. Comparison of the proposed harvester E-HE with other published work.

9.9 GHz, and 14.2 GHz). Simulation results showcase the harvester’s ability to efficiently capture EM power across incident angles, achieving over 95% E-HE at all resonance frequencies. A 3 × 3 array structure was fabricated and tested in an anechoic chamber to validate accuracy, demonstrating strong agreement between simulated and measured outcomes. Our proposed compact harvester has various practical uses, particularly for microelectronic devices. The small dimensions of this device make it well-suited for Internet of Things (IoT) devices, wearable health monitors, and smart home sensors. It allows for uninterrupted operation without the need for frequent recharging. Remote sensing utilizes it to provide consistent power to environmental and animal monitoring devices. This device’s multiband and polarization-insensitive design allows it to efficiently gather energy from several sources, making it an ideal choice for autonomous wireless sensors and low-power communication devices. This harvester prolongs the lifespan of electronics by utilizing ambient EM energy, hence decreasing dependence on conventional power sources and advocating for environmentally friendly technologies. Future research will explore advanced materials, optimize fabrication processes, and integrate with other technologies. Collaborations with industry and academia will accelerate innovation and practical deployment.

Data availability

The data supporting this study’s findings are available from the corresponding author upon reasonable request.

Received: 26 June 2024; Accepted: 12 August 2024

Published online: 16 August 2024

References

- Ball, A. D., Gu, F., Cattley, R., Wang, X. & Tang, X. Energy harvesting technologies for achieving self-powered wireless sensor networks in machine condition monitoring: A review. *Sensors* <https://doi.org/10.3390/s18124113> (2018).
- Tran, H. T., Nguyen, C. V., Nguyen, H. T. T. & Nguyen, M. T. Energy harvesting for devices in wireless sensor networks: A Review. *EAI Endorsed Trans. Internet Things* **9**(2), 1–11. <https://doi.org/10.4108/eetiot.v9i2.2953> (2023).
- Hemour, S. *et al.* Towards low-power high-efficiency RF and microwave energy harvesting. *IEEE Trans. Microw. Theory Tech.* **62**(4), 965–976. <https://doi.org/10.1109/TMTT.2014.2305134> (2014).
- Góra, P. & Łopato, P. Metamaterials' application in sustainable technologies and an introduction to their influence on energy harvesting devices. *Appl. Sci.* <https://doi.org/10.3390/app13137742> (2023).
- Ullah, N. *et al.* A compact-sized four-band metamaterial-based perfect absorber for electromagnetic energy harvesting applications. *Opt. Laser Technol.* **168**, 109836. <https://doi.org/10.1016/j.optlastec.2023.109836> (2023).
- Ullah, N. *et al.* An efficient, compact, wide-angle, wide-band, and polarization-insensitive metamaterial electromagnetic energy harvester. *Alex. Eng. J.* **82**, 377–388. <https://doi.org/10.1016/j.aej.2023.10.015> (2023).
- Ullah, N. *et al.* A compact complementary split ring resonator (CSRR) based perfect metamaterial absorber for energy harvesting applications. *Eng. Sci. Technol. Int. J.* **45**, 101473. <https://doi.org/10.1016/j.jestech.2023.101473> (2023).
- Bakir, M., Karaaslan, M., Dincer, F., Delihacioglu, K. & Sabah, C. Perfect metamaterial absorber-based energy harvesting and sensor applications in the industrial, scientific, and medical band. *Opt. Eng.* **54**(9), 097102. <https://doi.org/10.1117/1.oe.54.9.097102> (2015).
- Kaur, K. P., Upadhyaya, T., Palandoken, M. & Gocen, C. Ultrathin dual-layer triple-band flexible microwave metamaterial absorber for energy harvesting applications. *Int. J. RF Microw. Comput. Eng.* **29**(1), 1–7. <https://doi.org/10.1002/mmce.21646> (2019).
- Gunduz, O. & Sabah, C. Polarization angle independent perfect multiband metamaterial absorber and energy harvesting application. *J. Comput. Electron.* <https://doi.org/10.1007/s10825-015-0735-8> (2015).
- Evangeline Persis, G. P., John Paul, J., Bella Mary, T. & Catherine Joy, R. A compact tilted split ring multiband metamaterial absorber for energy harvesting applications. *Mater. Today Proc.* **56**, 368–372. <https://doi.org/10.1016/j.matpr.2022.01.206> (2022).
- Amer, A. A. G. *et al.* Dual-band, wide-angle, and high-capture efficiency metasurface for electromagnetic energy harvesting. *Nanomaterials* **13**(13), 1–16. <https://doi.org/10.3390/nano13132015> (2023).
- Fowler, C., Silva, S., Thapa, G. & Zhou, J. High efficiency ambient RF energy harvesting by a metamaterial perfect absorber. *Opt. Mater. Express* **12**(3), 1242. <https://doi.org/10.1364/ome.449494> (2022).
- Agrahari, R. *et al.* Triple-band metasurface absorber for RF energy harvesting applications. *Microw. Opt. Technol. Lett.* **65**(8), 2252–2261. <https://doi.org/10.1002/mop.33728> (2023).
- Akgol, O., Bağmancı, M., Karaaslan, M. & Ünal, E. Broad band MA-based on three-type resonator having resistor for microwave energy harvesting. *J. Microw. Power Electromagn. Energy* **51**(2), 134–149. <https://doi.org/10.1080/08327823.2017.1321928> (2017).
- Karaaslan, M. *et al.* Broad band metamaterial absorber based on wheel resonators with lumped elements for microwave energy harvesting. *Opt. Quantum Electron.* **50**(5), 1–18. <https://doi.org/10.1007/s1082-018-1484-2> (2018).
- Zhang, X., Liu, H. & Li, L. Electromagnetic power harvester using wide-angle and polarization-insensitive metasurfaces. *Appl. Sci.* **8**(4), 497. <https://doi.org/10.3390/app8040497> (2018).
- Lezec, H. J., Dionne, J. A. & Atwater, H. A. Negative refraction at visible frequencies. *Science* (80-) **316**(5823), 430–432. <https://doi.org/10.1126/science.1139266> (2007).
- Li, J., Yan, B., Liu, M. & Hu, X. Simultaneous normal and parallel incidence planar left-handed metamaterial. *Phys. Rev. E - Stat. Nonlinear Soft Matter Phys.* **80**(2), 8–13. <https://doi.org/10.1103/PhysRevE.80.026605> (2009).
- Kaur, K. P. & Upadhyaya, T. Performance evaluation of wide-angle ultrathin microwave metamaterial absorber with polarization independence. *Adv. Electromagn.* **7**(4), 71–77. <https://doi.org/10.7716/AEM.V7I4.761> (2018).
- Karaaslan, M., Bağmancı, M., Ünal, E., Akgol, O. & Sabah, C. Microwave energy harvesting based on metamaterial absorbers with multi-layered square split rings for wireless communications. *Opt. Commun.* **392**, 31–38. <https://doi.org/10.1016/j.optcom.2017.01.043> (2017).
- Chen, X., Grzegorzczak, T. M., Wu, B. I., Pacheco, J. & Kong, J. A. Robust method to retrieve the constitutive effective parameters of metamaterials. *Phys. Rev. E - Stat. Phys. Plasmas Fluids Relat. Interdiscip. Top.* **70**(1), 7. <https://doi.org/10.1103/PhysRevE.70.016608> (2004).
- Balanis, C. A. *Antenna Theory Analysis and Design*, Third Edition, p. 34 (2005).
- Ashoor, A. Z. & Ramahi, O. M. Polarization-independent cross-dipole energy harvesting surface. *IEEE Trans. Microw. Theory Tech.* **67**(3), 1130–1137. <https://doi.org/10.1109/TMTT.2018.2885754> (2019).
- Sun, H., Guo, Y. X., He, M. & Zhong, Z. Design of a high-efficiency 2.45-GHz rectenna for low-input-power energy harvesting. *IEEE Antennas Wirel. Propag. Lett.* **11**, 929–932. <https://doi.org/10.1109/LAWP.2012.2212232> (2012).
- Rappaport, T. S. *et al.* Overview of millimeter wave communications for fifth-generation (5G) wireless networks-with a focus on propagation models. *IEEE Trans. Antennas Propag.* **65**(12), 6213–6230. <https://doi.org/10.1109/TAP.2017.2734243> (2017).
- Ghaderi, B., Nayyeri, V., Soleimani, M. & Ramahi, O. M. Pixelated metasurface for dual-band and multi-polarization electromagnetic energy harvesting. *Sci. Rep.* **8**(1), 1–13. <https://doi.org/10.1038/s41598-018-31661-6> (2018).
- Costanzo, S. & Venneri, F. Polarization-insensitive fractal metamaterial surface for energy harvesting in IoT applications. *Electronics* <https://doi.org/10.3390/electronics9060959> (2020).
- Ahmed, A., Amer, G., Sapuan, S. Z. & Adel, Y. I. Efficient metasurface for electromagnetic energy harvesting with high capture efficiency and a wide range of incident angles. *J. Electromagn. Waves Appl.* <https://doi.org/10.1080/09205071.2022.2128898> (2022).
- Li, L. *et al.* Compact dual-band, wide-angle, polarization-angle-independent rectifying metasurface for ambient energy harvesting and wireless power transfer. *IEEE Trans. Microw. Theory Tech.* **69**(3), 1518–1528. <https://doi.org/10.1109/TMTT.2020.3040962> (2021).
- Shang, S., Yang, S., Shan, M., Liu, J. & Cao, H. High performance metamaterial device with enhanced electromagnetic energy harvesting efficiency. *AIP Adv.* <https://doi.org/10.1063/1.5002165> (2017).
- Almoneef, T. S., Erkmen, F. & Ramahi, O. M. Harvesting the energy of multi-polarized electromagnetic waves. *Sci. Rep.* **7**(1), 1–14. <https://doi.org/10.1038/s41598-017-15298-5> (2017).
- Yu, F., Yang, X., Zhong, H., Chu, C. & Gao, S. Polarization-insensitive wide-angle-reception metasurface with simplified structure for harvesting electromagnetic energy. *Appl. Phys. Lett.* <https://doi.org/10.1063/1.5046927> (2018).
- Erkmen, F. & Ramahi, O. M. A scalable, dual-polarized absorber surface for electromagnetic energy harvesting and wireless power transfer. *IEEE Trans. Microw. Theory Tech.* **69**(9), 4021–4028. <https://doi.org/10.1109/TMTT.2021.3087622> (2021).
- Polaiah, G., Krishnamoorthy, K., Kulkarni, M. Polarization-insensitive wide-angle reception triple-band metamaterial unit cell for electromagnetic energy harvesting. In: 2021 IEEE Indian Conf. Antennas Propagation, InCAP 2021, pp. 575–578, <https://doi.org/10.1109/InCAP52216.2021.9726308> (2021).

36. Duan, X., Chen, X., Zhou, Y., Zhou, L. & Hao, S. Wideband metamaterial electromagnetic energy harvester with high capture efficiency and wide incident angle. *IEEE Antennas Wirel. Propag. Lett.* **17**(9), 1617–1621. <https://doi.org/10.1109/LAWP.2018.2858195> (2018).
37. Ghaneizadeh, A., Mafinezhad, K. & Joodaki, M. Design and fabrication of a 2D-isotropic flexible ultra-thin metasurface for ambient electromagnetic energy harvesting. *AIP Adv.* <https://doi.org/10.1063/1.5083876> (2019).
38. Younesiraad, H., Niksan, O., Bemani, M. Highly-efficient double-sided dual-band polarization-independent metasurface energy harvester. In: 2020 28th Iran. Conf. Electr. Eng. ICEE 2020 (2020). <https://doi.org/10.1109/ICEE50131.2020.9261065>.

Acknowledgements

The authors would like to acknowledge the Telekom Malaysia Research & Development grant, RDTC 221039, MMUE/220015, TM, Malaysia. Also, they extend their appreciation to Taif University, Saudi Arabia, for supporting this work through project number (TU-DSPP-2024-11).

Author contributions

N.U.: Writing—original draft, Methodology, Investigation, Conceptualization. M.S.I.: Supervision, Software, Project administration, Funding acquisition. A.H.: Supervision, Formal analysis, validation. A.A.: Investigation, Validation. M.S.S.: Writing—review & editing, Funding acquisition. M.T.I.: Visualization, Resources, Project administration, Data curation.

Funding

This work is supported and funded by a Telekom Malaysia Research & Development grant, RDTC 221039, MMUE/220015, TM, Malaysia. Also, the research was funded by Taif University, Saudi Arabia, Project No. (TU-DSPP-2024-11).

Competing interests

The authors declare no competing interests.

Additional information

Correspondence and requests for materials should be addressed to M.S.I., A.H. or M.T.I.

Reprints and permissions information is available at www.nature.com/reprints.

Publisher's note Springer Nature remains neutral with regard to jurisdictional claims in published maps and institutional affiliations.

Open Access This article is licensed under a Creative Commons Attribution-NonCommercial-NoDerivatives 4.0 International License, which permits any non-commercial use, sharing, distribution and reproduction in any medium or format, as long as you give appropriate credit to the original author(s) and the source, provide a link to the Creative Commons licence, and indicate if you modified the licensed material. You do not have permission under this licence to share adapted material derived from this article or parts of it. The images or other third party material in this article are included in the article's Creative Commons licence, unless indicated otherwise in a credit line to the material. If material is not included in the article's Creative Commons licence and your intended use is not permitted by statutory regulation or exceeds the permitted use, you will need to obtain permission directly from the copyright holder. To view a copy of this licence, visit <http://creativecommons.org/licenses/by-nc-nd/4.0/>.

© The Author(s) 2024